Check for updates

Advanced Quantum Technologies

ADVANCED QUANTUM TECHNOLOGIES
www.advquantumtech.com

RESEARCH ARTICLE

Quantum Phase Transitions in Coherent Ising Machines: XY Model for Demonstration

Shuang-Quan Ma[1,2] | Jing-Yi-Ran Jin[1,2] | Qing Ai[1,2]

[1]School of Physics and Astronomy, Beijing Normal University, Beijing, China | [2]Key Laboratory of Multiscale Spin Physics (Beijing Normal University), Ministry of Education, Beijing, China

Correspondence: Qing Ai (aiqing@bnu.edu.cn)

Received: 29 January 2026 | **Revised:** 10 August 2026 | **Accepted:** 11 August 2026

Keywords: coherent Ising machines | optical parametric oscillators | quantum phase transitions | spectral mapping | XY model

ABSTRACT

In this work, we study the detection of quantum phase transitions (QPTs) in coherent Ising machines (CIMs) through a spectral mapping between the one-dimensional XY spin model and a network of degenerate optical parametric oscillators (DOPOs). This exact correspondence reveals that the DOPO spectrum faithfully encodes the critical behavior of anisotropic and isotropic XY chains, while a strongly anisotropic regime provides a controlled near-transverse-field-Ising realization, with the energy gap closing precisely at the critical point. The ground-state energy density and its derivatives are analyzed, and the resulting singularities in magnetic susceptibility accurately pinpoint the quantum critical points of the corresponding spin model. These results show that CIMs not only serve as powerful platforms for solving combinatorial optimization problems but also provide a versatile tool for probing universal quantum critical phenomena, bridging quantum-spin models and photonic quantum systems.

1 | Introduction

Quantum phase transitions (QPTs) mark fundamental changes in the ground state of a quantum many-body system, driven solely by quantum fluctuations at zero temperature. Unlike classical phase transitions, which arise from thermal fluctuations, QPTs occur when a control parameter (e.g., magnetic field or coupling strength) in the system's Hamiltonian is tuned across a critical point, leading to non-analytic behavior in the ground-state energy. This abrupt change reflects a reorganization of quantum correlations and often accompanies the closing of the energy gap in the thermodynamic limit [1, 2]. The study of QPTs not only illuminates the deep structure of quantum matter [3–8] but also bridges seemingly disparate fields such as condensed matter physics [9–13], quantum information science [14–17], and critical phenomena [18–21]. In particular, the enhanced quantum fluctuations and long-range entanglement near critical points offer novel mechanisms for quantum sensing [22–26], topological materials [27–29], and the engineering of exotic phases of matter [30–32]. As such, QPTs serve as both a theoretical cornerstone and a practical frontier in the exploration of strongly correlated quantum systems.

Building upon the theoretical framework of QPTs, the one-dimensional XY model provides an analytically accessible yet physically rich platform for exploring quantum critical phenomena [33–40]. The model captures essential features of quantum magnetism, such as competition between exchange interactions and external fields, while remaining exactly solvable. This solvability therefore enables the precise identification of quantum critical points, which are characterized by the closing of the energy gap and the emergence of universal scaling behavior. This universality likewise makes it a useful model for investigating quantum battery [41, 42] and quantum discord [43–45].

© 2026 Wiley-VCH GmbH

Experimentally, the quantum critical phenomena of the XY model can be accessed through the coherent Ising machine (CIM), which bridges its theoretical description with a tunable physical implementation. At its core, a CIM employs degenerate optical parametric oscillators (DOPOs) to simulate qubits, enabling efficient computation of the ground state. When the pump intensity surpasses the bifurcation threshold, the system undergoes a collective spontaneous symmetry breaking, driving it from the normal phase to the superradiant phase [46, 47]. Originally harnessed for solving Ising-based optimization problems [48–52], the nonlinear and collective dynamics of DOPO networks have since established CIMs as versatile simulators for quantum many-body phenomena, including phase transitions [53–56]. Beyond physics simulation, they are also used in many fields such as chemical synthesis [57, 58] and biology [59]. Recent experimental progress has also strengthened the practical basis for scalable and stable CIM. In particular, Wei et al. demonstrated a femtosecond-pumped CIM platform with stable operation over 8 h while solving a 100-vertex Möbius-ladder instance [60]. Such advances provide an important experimental foundation for future tests of the tunable DOPO-network protocol proposed here.

Following this introduction, the paper is organized as follows. In Section 2, we introduce the XY spin model and the DOPO network, and establish the spectral mapping between them. In Section 3, we present numerical results for the ground-state energy density and its derivatives, and discuss the simulated quantum critical phenomena. We conclude in Section 4 and provide an outlook on future directions.

2 | Model

2.1 | XY Model

The XY model represents a fundamental quantum spin system that exhibits rich critical behavior [1]. With $\hbar = 1$, the Hamiltonian for this model is given by

$$H_{\mathrm{XY}} = -\sum_{i=1}^{N}\left(J_x\sigma_i^x\sigma_{i+1}^x + J_y\sigma_i^y\sigma_{i+1}^y\right) - h\sum_{i=1}^{N}\sigma_i^z, \tag{1}$$

where J_x (J_y) denote the coupling strength along the x (y) direction, h represents the transverse field, and σ_i^α ($\alpha = x, y, z$) are the Pauli matrices.

To analyze this system, we first employ the Jordan–Wigner transformation [1] to map the spin operators to the fermionic operators as

$$\begin{aligned} \sigma_i^+ &= c_i^\dagger e^{i\pi\sum_{j=1}^{i-1}c_j^\dagger c_j},\\ \sigma_i^- &= c_i e^{-i\pi\sum_{j=1}^{i-1}c_j^\dagger c_j},\\ \sigma_i^z &= 2c_i^\dagger c_i - 1. \end{aligned} \tag{2}$$

Here σ_i^+ and σ_i^- denote the raising and lowering operators for the ith spin, defined as $\sigma_i^\pm = (\sigma_i^x \pm i\sigma_i^y)/2$. $c_i^\dagger$ (c_i) is the fermionic creation (annihilation) operator satisfying $\{c_i, c_j^\dagger\} = \delta_{ij}$. Transforming to momentum space under periodic boundary conditions, with $c_i = \sum_k e^{ikx_i}c_k/\sqrt{N}$ and $k = 2\pi m/N$ ($m = -N/2 + 1, \ldots, N/2$), the Hamiltonian becomes

$$\begin{aligned} H'_{\mathrm{XY}} = -\sum_k \Big\{ & i(J_x - J_y)\sin k(c_k^\dagger c_{-k}^\dagger + c_k c_{-k}) \\ & - 2[(J_x + J_y)\cos k + h]c_k^\dagger c_k\Big\} + hN. \end{aligned} \tag{3}$$

After performing the Bogoliubov transformation [1], we can diagonalize the Hamiltonian as

$$H'_{\mathrm{XY}} = \sum_k E_k^{\mathrm{XY}}\gamma_k^\dagger\gamma_k + E_0^{\mathrm{XY}}, \tag{4}$$

in which $\gamma_k^\dagger$ (γ_k) represent the Bogoliubov quasiparticle creation (annihilation) operators. The corresponding energy spectrum and ground-state energy are

$$\begin{aligned} E_k^{\mathrm{XY}} &= 2\sqrt{[h + (J_x + J_y)\cos k]^2 + [(J_x - J_y)\sin k]^2},\\ E_0^{\mathrm{XY}} &= -\frac{1}{2}\sum_k E_k^{\mathrm{XY}}, \end{aligned} \tag{5}$$

respectively.

In the thermodynamic limit, i.e., $N \to \infty$, the energy density of the ground state becomes

$$e_g^{\mathrm{XY}} = \lim_{N\to\infty}\frac{E_0^{\mathrm{XY}}}{N} = -\frac{1}{2\pi}\int_0^\pi E_k^{\mathrm{XY}}dk. \tag{6}$$

The critical points where the QPT occurs can be identified by examining the closure of the energy gap, i.e., $\min_k(E_k^{XY}) = 0$. This leads to the conditions, i.e.,

$$\begin{aligned} h + (J_x + J_y)\cos k &= 0,\\ (J_x - J_y)\sin k &= 0, \end{aligned} \tag{7}$$

which should be satisfied simultaneously. This analysis reveals several important cases. For the isotropic XY model, i.e., $J_x = J_y = J$, the condition shown in Equation (7) is simplified as

$$h + 2J\cos k = 0. \tag{8}$$

The critical points occur at $h_c = \pm 2J$, as $\cos k \in [-1, 1]$, where the system enters the fully z-polarized paramagnetic phase. This symmetric behavior reflects the rotational invariance of the isotropic model. In the general case with anisotropic couplings, i.e., $J_x \neq J_y$, the condition shown in Equation (7) requires $\sin k = 0$, namely, $k = 0$ or $k = \pi$, leading to the critical fields as

$$\begin{aligned} h_c &= -(J_x + J_y), \quad \text{for } k = 0,\\ h_c &= J_x + J_y, \quad \text{for } k = \pi. \end{aligned} \tag{9}$$

The critical behavior thus depends on the sum of the two coupling constants. The TFI model is an important special case, i.e., $J_y = 0$ and $J_x = J > 0$, which yields

$$h_c = -J, \quad \text{for } k = 0,$$

25119044, 2026, 9, Downloaded from https://advanced.onlinelibrary.wiley.com/doi/10.1002/qute.70428 by Beijing Normal University, Wiley Online Library on [02/09/2026]. See the Terms and Conditions (https://onlinelibrary.wiley.com/terms-and-conditions) on Wiley Online Library for rules of use; OA articles are governed by the applicable Creative Commons License

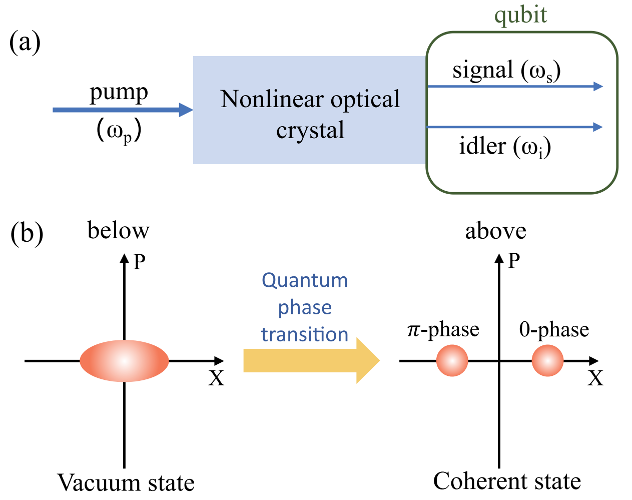

FIGURE 1 | (a) Schematic representation of a DOPO, a key component for constructing a CIM. (b) Simplified phase-space illustration of a DOPO showing the vacuum state below the threshold and the two coherent states with phases 0 and π above the threshold.

$$h_c = J, \quad \text{for } k = \pi. \tag{10}$$

For simplicity, we adopt the convention of a positive transverse field $h > 0$ throughout this work. Under this convention, the QPT driven by increasing h from zero occurs at the critical field $h_c = J_x + J_y$, which corresponds to the gap closing at momentum $k = \pi$ as given in Equation (9). This marks the transition from a ferromagnetically ordered phase to a paramagnetic phase. The alternative critical point $h_c = -(J_x + J_y)$ for $k = 0$ corresponds to a negative transverse field; it is physically equivalent to the positive-field case under a global spin rotation (e.g., a π rotation around the x-axis flips the sign of h).

2.2 | Network of N-DOPOs

In an OPO with second-order nonlinear effects, a pump field at frequency ω_p undergoes parametric down-conversion within the nonlinear medium, yielding a signal field with frequency ω_s and an idler field with frequency ω_i. In the degenerate regime considered in this work, the signal and idler frequencies are identical, i.e., $\omega_s = \omega_i = \omega_p/2$. As illustrated in Figure 1a, the Hamiltonian of the system can be expressed as

$$H_{\text{D}} = H_0 + H_{\text{int}}, \tag{11}$$

where

$$H_0 = \omega_s a_s^\dagger a_s + \omega_p a_p^\dagger a_p, \tag{12}$$

$$H_{\text{int}} = i\frac{\kappa}{2} a_s^{\dagger 2} a_p + i\varepsilon a_p^\dagger e^{-i\omega_p t} + \text{H.c.} \tag{13}$$

Here $a_s^\dagger$ (a_s) and $a_p^\dagger$ (a_p) are the creation (annihilation) operators for the signal and pump fields, respectively. The coupling constant κ quantifies the strength of the second-order nonlinear interaction, and ε is the amplitude of the external coherent drive applied to the pump mode. When there is a detuning $\Delta = \omega_s - (\omega_p/2)$ between the signal and the pump fields, with respect to the free Hamiltonian

$$H_f = \frac{\omega_p}{2} a_s^\dagger a_s + \omega_p a_p^\dagger a_p, \tag{14}$$

the Hamiltonians are transformed to the interaction picture as

$$H_0' = \Delta a_s^\dagger a_s, \tag{15}$$

$$H_{\text{int}}' = i\frac{\kappa}{2} a_s^{\dagger 2} a_p + i\varepsilon a_p^\dagger + \text{H.c.} \tag{16}$$

Following the Heisenberg–Langevin approach [61], the temporal evolution of the pump field is described by

$$\frac{da_p}{dt} = -\gamma_p a_p + \varepsilon - \frac{\kappa}{2} a_s^2, \tag{17}$$

where γ_p represents the decay rate of the pump mode. Assuming the pump field reaches its steady state rapidly, we adiabatically eliminate it to obtain an effective Hamiltonian for the signal mode as

$$H_{\text{D}} = \Delta a^\dagger a + i\frac{\kappa\varepsilon}{2\gamma_p} a^{\dagger 2} + \text{H.c.} \tag{18}$$

Hereafter, we omit the subscript s for the signal field for simplicity.

Extending this description to N nearest-neighbor-coupled DOPOs yields the generalized Hamiltonian

$$H_{\text{ND}} = \sum_{i=1}^{N} \Delta a_i^\dagger a_i + \sum_{i=1}^{N} \left(i\frac{\kappa\varepsilon}{2\gamma_p} a_i^{\dagger 2} - J a_i^\dagger a_{i+1} \right) + \text{H.c.}, \tag{19}$$

where $a_i^\dagger$ (a_i) is the creation (annihilation) operator for the ith DOPO, and J quantifies the coupling strength between two adjacent DOPOs. To diagonalize H_{ND}, we first move to momentum space via a Fourier transformation, which brings the Hamiltonian into the form

$$H_{\text{ND}}' = \sum_k \left(\epsilon_k a_k^\dagger a_k + i\frac{\kappa\varepsilon}{2\gamma_p} a_k^\dagger a_{-k}^\dagger + \text{H.c.} \right), \tag{20}$$

where we have defined $\epsilon_k = \Delta - 2J\cos k$ for brevity. A subsequent Bogoliubov transformation

$$b_k = a_k \cosh r_k + a_{-k}^\dagger e^{i\theta} \sinh r_k \tag{21}$$

is then applied, where the parameters are chosen as $\tanh(2r_k) = |\kappa\varepsilon|/(\gamma_p \epsilon_k)$ and $\theta = \arg(\kappa\varepsilon) + \pi/2$ to remove off-diagonal terms. The resulting diagonal Hamiltonian is

$$H_{\text{ND}}' = \sum_k \Omega_k b_k^\dagger b_k + \frac{1}{2}\sum_k (\Omega_k - \epsilon_k), \tag{22}$$

where the quasiparticle energy spectrum reads

$$\Omega_k = \sqrt{\epsilon_k^2 - \left|\frac{\kappa\varepsilon}{\gamma_p}\right|^2}, \tag{23}$$

25119044, 2026, 9, Downloaded from https://advanced.onlinelibrary.wiley.com/doi/10.1002/qute.70428 by Beijing Normal University, Wiley Online Library on [02/09/2026]. See the Terms and Conditions (https://onlinelibrary.wiley.com/terms-and-conditions) on Wiley Online Library for rules of use; OA articles are governed by the applicable Creative Commons License

and the second sum corresponds to the zero-point energy contribution.

In this framework, the DOPO network exhibits a QPT from a normal phase (vacuum state) to a symmetry-broken phase (coherent state) when the pump intensity exceeds the threshold, as shown in Figure 1b. Although the intrinsic threshold transition of a DOPO involves a $\mathbb{Z}_2$ symmetry breaking that is mathematically reminiscent of magnetic ordering, it is distinct from the XY-model quantum criticality considered below. In our scheme, the CIM is operated in its above-threshold regime, while the critical behavior of the XY model is encoded through the engineered spectrum of the DOPO network.

2.3 | Energy-Spectrum Matching

We now present a rigorous mapping between the energy spectra of the XY model and that of the N-DOPO network. Defining $J_s = J_x + J_y$, $J_d = J_x - J_y$, and $D = \left|\kappa\varepsilon/\gamma_p\right|$, the squared energy spectrum of the XY model is given by

$$(E_k^{\mathrm{XY}})^2 = 4(h^2 + J_d^2) + 8J_s h \cos k + 16 J_x J_y \cos^2 k. \tag{24}$$

Meanwhile, the squared energy spectrum of the DOPO network reads

$$\Omega_k^2 = \Delta^2 - D^2 - 4\Delta J \cos k + 4J^2 \cos^2 k. \tag{25}$$

Requiring the two spectra to coincide for all k, we obtain the exact mapping

$$\begin{aligned} J &= 2\sqrt{J_x J_y}, \\ \Delta &= -\frac{hJ_s}{\sqrt{J_x J_y}}, \\ D^2 &= J_d^2\left(\frac{h^2}{J_x J_y} - 4\right). \end{aligned} \tag{26}$$

Through this transformation, the critical behavior of the XY model can be faithfully studied in the DOPO network. For the anisotropic case $J_x \neq J_y$, it requires $D^2 \geq 0$. For a positive transverse field $h > 0$, this condition yields

$$h \geq h_{\min} = 2\sqrt{J_x J_y}. \tag{27}$$

Therefore, the present DOPO mapping does not cover the regime from $h = 0$ to $h_{\min}$. Instead, it provides an exact spectral realization in an experimentally-accessible regime from a field slightly lower than the critical point to a strong field. Importantly, the quantum critical point always lies within the accessible domain because

$$h_c = J_x + J_y \geq 2\sqrt{J_x J_y} = h_{\min}. \tag{28}$$

Thus, the closing of the energy gap can always be captured by the proposed DOPO network. For the near-TFI example adopted in the original manuscript, i.e., $J_x = 1$ and $J_y = 0.01$, one obtains $h_{\min} = 0.2 < h_c = 1.01$, which shows that the critical point, together with two phases on both its sides, remains accessible. Nevertheless, the deep in the ferromagnetically ordered phase along x direction, i.e., $0 \leq h < h_{\min}$, can not be directly observed by the present mapping. In the thermodynamic limit, the energy density satisfies

$$e_g^{\mathrm{D}} = -e_g^{\mathrm{XY}} + \frac{hJ_s}{2\sqrt{J_x J_y}}. \tag{29}$$

This relationship implies that the non-analyticities in the ground-state energy of the XY model, which characterize the QPT, are directly inherited by the DOPO network, albeit with a linear shift and scaling.

We next clarify whether the parameter variation required by the spectral mapping can drive an intrinsic dissipative bifurcation of the DOPO network. In a realistic optical system, the signal mode has a nonvanishing decay rate γ_s. For each k-mode in Equation (20), the equation of motion can be written as

$$\frac{d}{dt}\begin{pmatrix} a_k \\ a_{-k}^{\dagger} \end{pmatrix} = \begin{pmatrix} -\gamma_s - i\varepsilon_k & D \\ D & -\gamma_s + i\varepsilon_k \end{pmatrix}\begin{pmatrix} a_k \\ a_{-k}^{\dagger} \end{pmatrix}. \tag{30}$$

The eigenvalues of the drift matrix are

$$\lambda_{k,\pm} = -\gamma_s \pm \sqrt{D^2 - \epsilon_k^2}. \tag{31}$$

Consequently, throughout the entire accessible mapping parameter regime, the drift eigenvalues can be written as $\lambda_{k,\pm} = -\gamma_s \pm i\Omega_k$ and hence $\mathrm{Re}\lambda_{k,\pm} = -\gamma_s < 0$. Therefore, no drift eigenvalue crosses the imaginary axis and no additional steady-state branch emerges as the mapped parameters are varied. The DOPO network therefore remains within the same dynamically stable degenerate parametric regime. At the critical point of the mapped XY model, the $k = \pi$ mode satisfies $\Omega_\pi = 0$. Nevertheless, the corresponding drift eigenvalues remain

$$\lambda_{\pi,+} = \lambda_{\pi,-} = -\gamma_s < 0, \tag{32}$$

so the mapped gap-closing condition does not represent a dissipative instability of the DOPO network. The actual parametric-oscillation threshold would instead be determined by $\lambda_{k,+} = 0$, which gives

$$D^2 = \epsilon_k^2 + \gamma_s^2. \tag{33}$$

This threshold is never reached along the mapped parameter regime because

$$\epsilon_k^2 + \gamma_s^2 - D^2 = \Omega_k^2 + \gamma_s^2 > 0. \tag{34}$$

In particular, even at $\Omega_\pi = 0$, the system remains distinguished from the threshold of the DOPO by the nonvanishing γ_s^2. This situation is fundamentally different from the detuning-induced spectral phase transition reported for optical parametric oscillators in Refs. [62, 63]. In that work, tuning the cavity phase detuning $\Delta\phi$ changes the oscillation selected by the OPO from a degenerate regime, in which the signal and idler overlap at the half-harmonic frequency ω_0, to a non-degenerate regime with two distinct frequency branches $\omega_0 \pm \delta\omega$. The square-root splitting

25119044, 2026, 9, Downloaded from https://advanced.onlinelibrary.wiley.com/doi/10.1002/qute.70428 by Beijing Normal University, Wiley Online Library on [02/09/2026]. See the Terms and Conditions (https://onlinelibrary.wiley.com/terms-and-conditions) on Wiley Online Library for rules of use; OA articles are governed by the applicable Creative Commons License

of these branches therefore represents a transition between two spectral regimes of the OPO itself.

By contrast, the DOPOs considered in the present mapping remain in the degenerate parametric configuration throughout the mapped parameter trajectory. Varying the mapped detuning Δ, together with the parametric amplitude D according to Equation (26), does not produce signal–idler frequency splitting, steady-state branch switching, or a transition into a non-degenerate OPO regime. Moreover, the momentum k in our model labels a spatial normal mode of the coupled-DOPO network, rather than the optical signal–idler frequency offset $\delta\omega$ considered in Ref. [62]. Therefore, $\Omega_\pi = 0$ describes the softening of the mapped $k = \pi$ network mode and not a degenerate-to-nondegenerate transition of the optical system.

Having established that the mapped parameter regime does not cross the dissipative bifurcation threshold, we next examine how finite loss modifies the experimentally observable signature of the mapped XY critical point. Although the DOPO network remains within the same stable regime, the decay rate γ_s changes the real-valued Bogoliubov frequencies into complex response poles and provides a finite linewidth. After performing a Fourier transformation, i.e., $a_k(t) = \int \frac{d\omega}{2\pi} a_k(\omega) e^{-i\omega t}$, the corresponding response function [64] is

$$\chi_k(\omega) = \frac{1}{(\gamma_s - i\omega)^2 + \Omega_k^2} \begin{pmatrix} \gamma_s - i(\omega + \varepsilon_k) & D \\ D & \gamma_s - i(\omega - \varepsilon_k) \end{pmatrix}. \tag{35}$$

Thus, the ideal gap closing of the mapped XY model appears in the dissipative DOPO as a softening of the response pole, while the finite decay rate γ_s provides a linewidth. In particular, at the critical momentum $k = \pi$ and at zero frequency, the soft-mode response can be characterized by

$$R_\pi(0) \propto \frac{1}{\gamma_s^2 + \Omega_\pi^2}. \tag{36}$$

Therefore, the divergence expected in the closed XY model is rounded into a finite response peak in the dissipative DOPO system. The peak height and width are controlled by γ_s, while the peak position still identifies the mapped XY critical point through $\Omega_\pi = 0$. In this case, a broadened spectral functional can be written as

$$\tilde{e}_g^{\mathrm{D}} = -\frac{1}{2\pi} \int_0^\pi \sqrt{\Omega_k^2 + \gamma_s^2}\, dk. \tag{37}$$

Its second derivative provides a convenient measure of the dissipatively broadened susceptibility, rather than a thermodynamic ground-state susceptibility of the DOPO system itself. The phase assignment is made by first using the mapping relation, i.e., Equation (26), to reconstruct the effective transverse field of the corresponding XY model,

$$h_{\mathrm{eff}} = -\Delta \frac{\sqrt{J_x J_y}}{J_x + J_y}. \tag{38}$$

Then h_{eff} is compared with the critical point h_c. For $h_{\mathrm{eff}} < h_c$, the mapped closed XY model lies on the ordered side. For $h_{\mathrm{eff}} > h_c$, it lies in the paramagnetic phase, and the critical point is identified by $h_{\mathrm{eff}} = h_c$, which coincides with the soft-mode condition $\Omega_\pi = 0$.

3 | Results and Discussion

As illustrated in Figure 2, we consider three quantum spin-chain models: the anisotropic XY model with parameters $J_x = 2$ and $J_y = 1$, the isotropic XY model with $J_x = J_y = 1$, and the TFI model with $J_x = 1$ and $J_y = 0$. The anisotropic XY and TFI models exhibit Ising-type second-order QPT driven by the transverse field. The isotropic XY model represents the $U(1)$-symmetric limit, where the spectrum is gapless for $|h| \le 2J$ and the positive-field boundary $h_c = 2J$ marks the transition into the fully polarized paramagnetic phase. In the thermodynamic limit, the TFI model and the anisotropic XY model with $J_x > J_y$ possess a symmetry-broken ordered phase at small h, characterized by a nonzero x-direction order parameter m_x. In contrast, the isotropic XY model has a $U(1)$ spin-rotation symmetry about the z axis and forms a gapless critical phase for $|h| < 2J$, with $m_z = 0$ at $h = 0$. As h increases from zero, the ground-state energy density e_g^{XY} and the longitudinal magnetization m_z^{XY} evolve continuously. At the critical field strength $h_c = J_x + J_y$, each system undergoes a QPT into a paramagnetic phase, where the spins become predominantly aligned along the field direction. For $h > h_c$, the longitudinal magnetization m_z increases monotonically toward its saturation value of $+1$, whereas the transverse components m_x and m_y are suppressed to zero. The magnetic susceptibility χ^{XY} displays a divergence near h_c, directly signaling the critical point. For the isotropic XY model in the paramagnetic phase, the first derivative of the ground-state energy density remains constant, leading to a vanishing second derivative. This accounts for the disappearance of its corresponding curve beyond h_c in the logarithmic-scale plot of Figure 2c. Collectively, this systematic analysis provides a clear physical interpretation and numerical verification for the simulation of quantum critical phenomena using a CIM.

The simulated ground-state properties of the DOPO network are presented in Figure 3. The three columns correspond to different regimes of the XY model mapped onto the optical system. The left column, with parameters $J = 2\sqrt{2}$ and $\Delta = -3h/\sqrt{2}$, represents the anisotropic XY model. The middle column, with $J = 2$, $\Delta = -2h$, and $D = 0$, corresponds to the isotropic XY model. The right column approximates the TFI limit using a strongly anisotropic XY model with $J_y \ll J_x$. For concreteness, taking $J_x = 1$ and $J_y = 0.01$, the mapping in Equation (26) gives $J = 0.2$ and $\Delta = -10.1h$. For finite $J_y > 0$, the mapping guarantees an exact equality $\Omega_k = E_k^{XY}$ for the corresponding anisotropic XY chain. Therefore, in the anisotropic and isotropic cases the gap closing of the XY model is exactly mapped onto the spectrum of the DOPO. In the right column, $J_y = 0.01$ gives a realization of the quasi-TFI, whose convergence toward the strict TFI spectrum is analyzed below in Figure 4. The vertical dashed line in the figure marks $\Delta_c = -2J - D$, which corresponds precisely to this critical point and manifests as a divergence of the susceptibility χ^{D}. It is worth noting that, under the mapping, both Δ and D vary together with h, and the system always satisfies $\epsilon_k^2 \ge D^2$. Even at Δ_c, where the gap closes, the system merely touches the phase boundary. The middle column, corresponding to the isotropic limit $J_x = J_y$, is a limiting case of the mapping with $D = 0$. In this limit

25119044, 2026, 9, Downloaded from https://advanced.onlinelibrary.wiley.com/doi/10.1002/qute.70428 by Beijing Normal University, Wiley Online Library on [02/09/2026]. See the Terms and Conditions (https://onlinelibrary.wiley.com/terms-and-conditions) on Wiley Online Library for rules of use; OA articles are governed by the applicable Creative Commons License

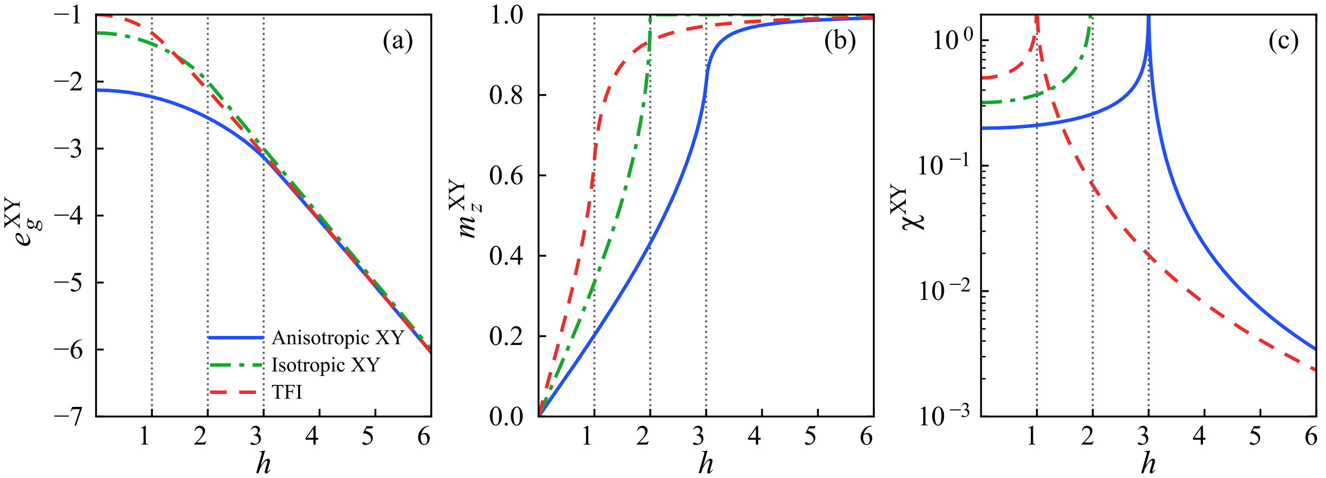

FIGURE 2 | Numerical results for three quantum-spin-chain models under an external field h: (a) Ground-state energy density e_g^{XY}, (b) magnetization $m_z^{\mathrm{XY}} = -\partial e_g^{\mathrm{XY}}/\partial h$, and (c) magnetic susceptibility $\chi^{\mathrm{XY}} = -\partial^2 e_g^{\mathrm{XY}}/\partial h^2$. Note that sub-figure (c) uses a logarithmic scale. The curves correspond to the anisotropic XY model ($J_x = 2, J_y = 1$, blue solid line), the isotropic XY model ($J_x = J_y = 1$, green dash-dotted line), and the transverse-field Ising model ($J_x = 1, J_y = 0$, red dashed line). The vertical dotted lines mark the calculated critical fields h_c for each model.

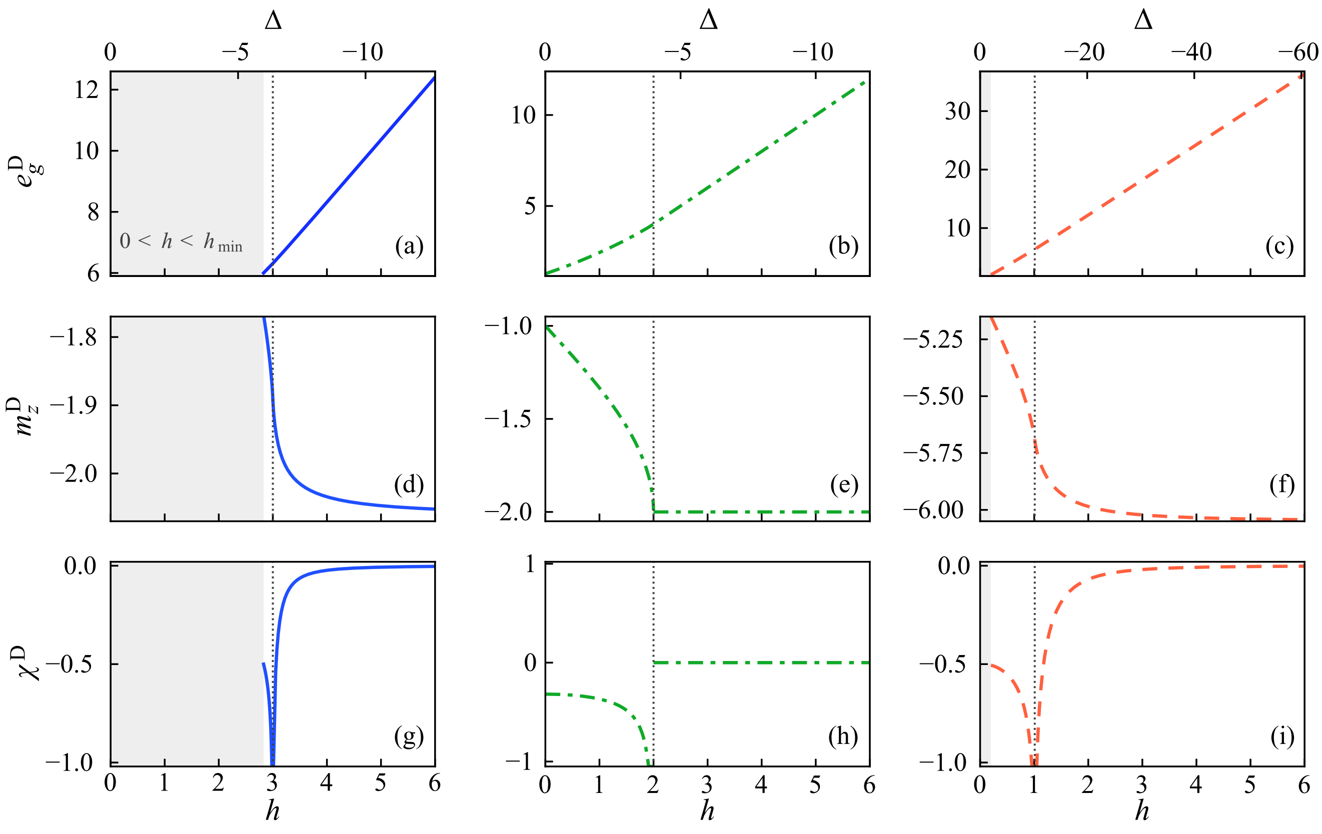

FIGURE 3 | The spectral signatures of the mapped XY critical points in the representation of the DOPO network. Columns show DOPO parameter regimes: (left) $J = 2\sqrt{2}, \Delta = -3h/\sqrt{2}$; (middle) $J = 2, \Delta = -2h$; (right) $J = 0.2, \Delta = -10.1h$. These correspond to anisotropic XY, isotropic XY, and near-TFI spin chains, respectively. From top to bottom, the panels display: (a–c) the ground-state energy density e_g^{D}; (d–f) the longitudinal magnetization m_z^{D}; and (g–i) the magnetic susceptibility χ^{D}. Each panel features dual horizontal axes: the upper axis shows the DOPO detuning parameter Δ, and the lower axis shows the corresponding transverse field h in the XY model. Vertical dashed lines indicate the critical points at $\Delta_c = -2J - D$. In addition, the gray-shaded regions denote the field interval $0 < h < h_{\min} = 2\sqrt{J_x J_y}$, where $D^2 < 0$ and the present finite-parameter DOPO mapping admits no real parametric-drive amplitude. The shading therefore marks an optically inaccessible region of the mapping, rather than an absent phase of the XY model. For the isotropic case $J_x = J_y$, $D = 0$ and no such restriction arises.

25119044, 2026, 9, Downloaded from https://advanced.onlinelibrary.wiley.com/doi/10.1002/qute.70428 by Beijing Normal University, Wiley Online Library on [02/09/2026]. See the Terms and Conditions (https://onlinelibrary.wiley.com/terms-and-conditions) on Wiley Online Library for rules of use; OA articles are governed by the applicable Creative Commons License

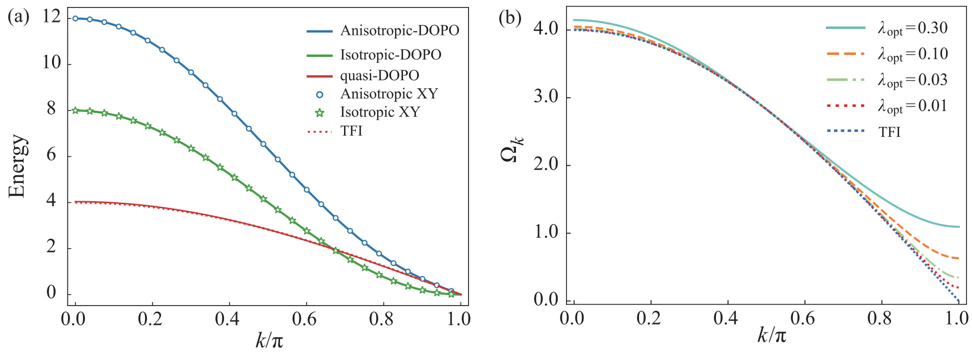

FIGURE 4 | Energy-spectrum correspondence between the DOPO network and the XY-family spin models. (a) Exact spectral matching between the DOPO quasiparticle spectra and the corresponding anisotropic XY, isotropic XY, and TFI spin-chain spectra at the critical point, i.e., $h = J_x + J_y$. For the anisotropic XY model, the parameters are $J_x = 2, J_y = 1$, while the corresponding parameters for the DOPO are $J = 2\sqrt{2}, \Delta = -9/\sqrt{2}$ and $D^2 = 0.45$. For the isotropic XY model, the parameters are $J_x = 1$ and $J_y = 1$, while the corresponding parameters for the DOPO are $J = 2, \Delta = -6$ and $D^2 = 0$. For the TFI model, the parameters are $J_x = 1$ and $J_y = 0$, while the corresponding parameters for the DOPO are $J = 0.2$ ($J_y = 0.01$), $\Delta = -10.1$ and $D^2 = 96.06$. For the first two cases, the mapping $\Omega_k = E_k^{XY}$ can be exactly fulfilled. For the TFI model, the energy spectrum of the DOPO is quite close to that of the TFI model. (b) The convergence of the DOPO spectrum toward the TFI spectrum as $\lambda_{\mathrm{opt}} \to 0$. The intrinsic optical ratio $\lambda_{\mathrm{opt}} = 2J/|\Delta_c|$ is related to the XY anisotropy ratio by $\lambda_{\mathrm{opt}} = 4\eta/(1+\eta)^2$, where $\eta = J_y/J_x$. Hence, decreasing λ_{opt} from 0.30 to 0.01 corresponds to a systematic reduction of J_y/J_x and thus to an approach toward the TFI limit. The progressive suppression of the deviation near $k = \pi$ and $k = 0$ demonstrates the convergence of the quasi-TFI DOPO realization of the exact TFI spectrum.

the parametric-amplification term vanishes, and the mapped spectrum is realized by the linear detuned oscillator network. These results demonstrate that the critical point of the XY model can be located by measuring the susceptibility χ^{D} of the DOPO network, thereby providing a feasible scheme for experimental studies of the QPT in the XY model on a CIM platform.

Because the strict TFI point $J_y = 0$ is singular in the finite-parameter mapping of the DOPO, the right column of Figure 3 should be understood as a quasi-TFI realization rather than as an exact finite-parameter TFI mapping.

To quantify this approximation, we perform a convergence analysis in Figure 4. As shown in Figure 4a, the spectral mapping between the DOPO network and the corresponding XY chain is almost exact. The issue is therefore not the validity of the mapping at $J_y = 0.01$, but rather the convergence of this strongly-anisotropic XY model toward the exact TFI spectrum with $J_y = 0$. To show this convergence explicit, we introduce $\eta = J_y/J_x$ and demonstrate that the parameter used in Figure 4b satisfies

$$\lambda_{\mathrm{opt}} = \frac{4\eta}{(1+\eta)^2} \tag{39}$$

with $\lambda_{\mathrm{opt}} = 2J/|\Delta_c|$, at the critical point. Therefore, decreasing λ_{opt} in Figure 4b is equivalent to a systematic reduction of η. The progressive convergence of the DOPO spectra toward the exact TFI spectrum near $k = \pi$ and $k = 0$ demonstrates that the DOPO realization of the quasi-TFI continuously approaches the exact TFI spectrum as $\eta \to 0$. From an experimental perspective, the quasi-TFI regime should be understood as a finite-anisotropy approximation rather than the singular limit $\eta \to 0$. Therefore, approaching the strict TFI limit increases the required dynamic range between the detuning and parametric drive on the one hand and the inter-DOPO coupling on the other. In practice, the achievable tuning range and the finite linewidth γ_s of the signal mode set a lower bound on how small η can be made. Therefore, the smallest values of λ_{opt} shown in Figure 4b are intended to illustrate the asymptotic convergence toward the TFI limit, rather than to prescribe experimentally-required operating points. Consequently, a finite anisotropy, such as $\eta = 0.01$, provides a controlled quasi-TFI realization without requiring access to the singular optical limit. Recent CIM experiments have demonstrated programmable coupling, pump control, and long-term cavity stabilization, providing an experimental basis for exploring such finite quasi-TFI regimes [49, 50, 60].

To further clarify the role of dissipation, we now analyze the dissipative response of the mapped DOPO network. Figure 5 shows the dissipative-DOPO signatures of the mapped XY-family spin models. As shown in Figure 5a–c, the broadened susceptibility $\tilde{\chi}^D$ exhibits a clear peak when h_{eff} approaches h_c. The same critical point is also identified by the response in Figure 5d–f. At the critical point of the mapped XY, the $k = \pi$ mode satisfies $\Omega_\pi = 0$, leading to an enhanced response. For $\gamma_s = 0$, this expression formally diverges at $h_{\mathrm{eff}} = h_c$. In the plotted curves, this ideal divergence is represented by the sharpest peak, while finite γ_s broadens it into a finite-height response peak.

The comparison between the upper and lower rows of Figure 5 shows that $\tilde{\chi}^D$ and $R_\pi(0)$ locate the same critical field for all three mappings. Increasing γ_s broadens the anomaly and suppresses the peak height, but it does not shift the position of the critical response. Therefore, the dissipative DOPO network retains the ability to identify the critical point of the corresponding closed XY model, even though the ideal gap-closing singularity is replaced by a finite-linewidth optical response. Based on this local critical response, Figure 6 further illustrates how the dissipative response of the DOPO can be used to identify the phases of the XY model. Figure 6a shows the phase diagram of the XY model in the normalized parameter space $(g, J_d/J_s)$, where $g = h/J_s$. In the ordered regime $g < 1$, the ferromagnetic ordering direction is selected by the sign of J_d/J_s. Positive J_d/J_s leads to the FM-

25119044, 2026, 9, Downloaded from https://advanced.onlinelibrary.wiley.com/doi/10.1002/qute.70428 by Beijing Normal University, Wiley Online Library on [02/09/2026]. See the Terms and Conditions (https://onlinelibrary.wiley.com/terms-and-conditions) on Wiley Online Library for rules of use; OA articles are governed by the applicable Creative Commons License

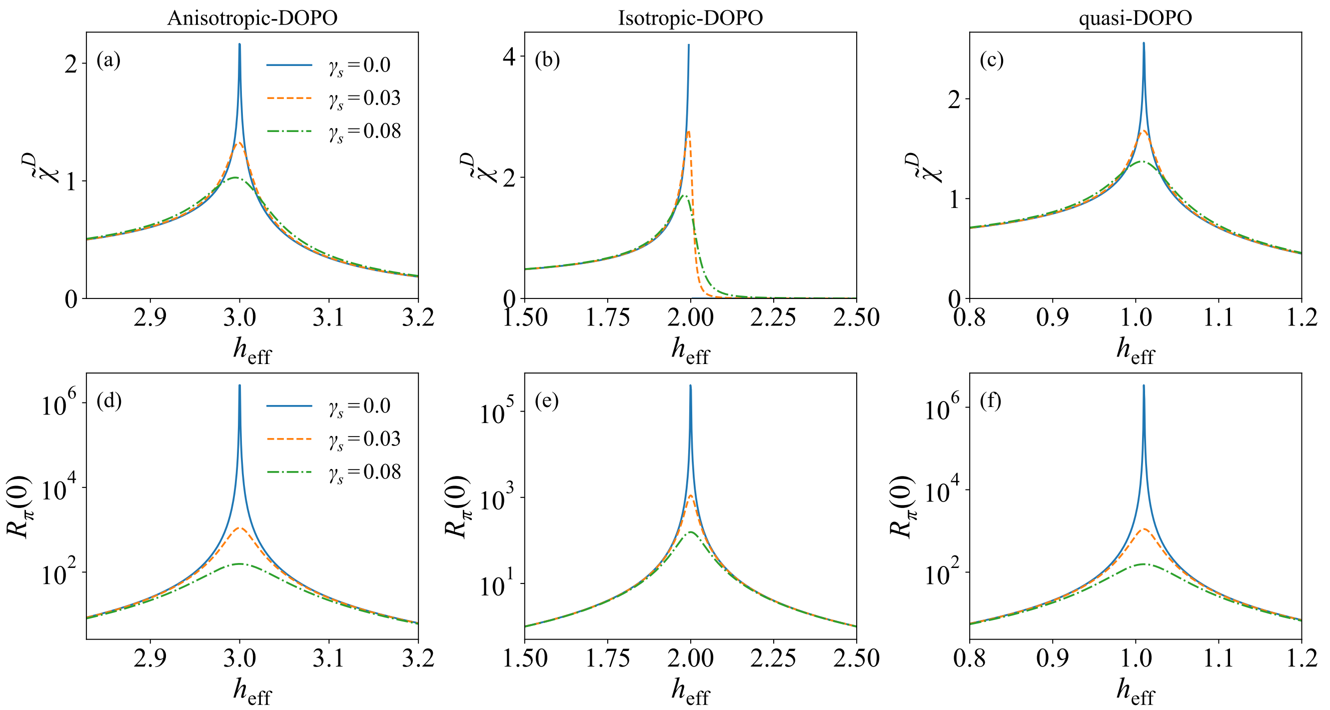

FIGURE 5 | Dissipative-DOPO signatures of quantum critical behavior in the mapped XY-family spin models. Panels (a)–(c) show the broadened susceptibility $\tilde{\chi}^D$, i.e., the second derivative of the rescaled energy $\tilde{e}_g^D$ of the ground state, for the anisotropic-XY, isotropic-XY, and quasi-TFI mappings, respectively. Panels (d)–(f) show the corresponding obscured-mode response $R_\pi(0)$ at $k = \pi$. The horizontal axis is the effective transverse field h_{eff}, reconstructed from the detuning of the DOPO through the spectral mapping. Different line styles denote different dissipation rates γ_s of the signal mode, and the vertical dotted lines mark the critical field h_c of the corresponding XY model. As h_{eff} approaches h_c, both $\tilde{\chi}^D$ and $R_\pi(0)$ develop distinct peaks, indicating that the dissipative linear response of the DOPO can locate the critical point of the mapped XY model. For $\gamma_s = 0$, $R_\pi(0)$ formally diverges at $\Omega_\pi = 0$, whereas a nonvanishing γ_s broadens this ideal singularity into a finite-height response peak.

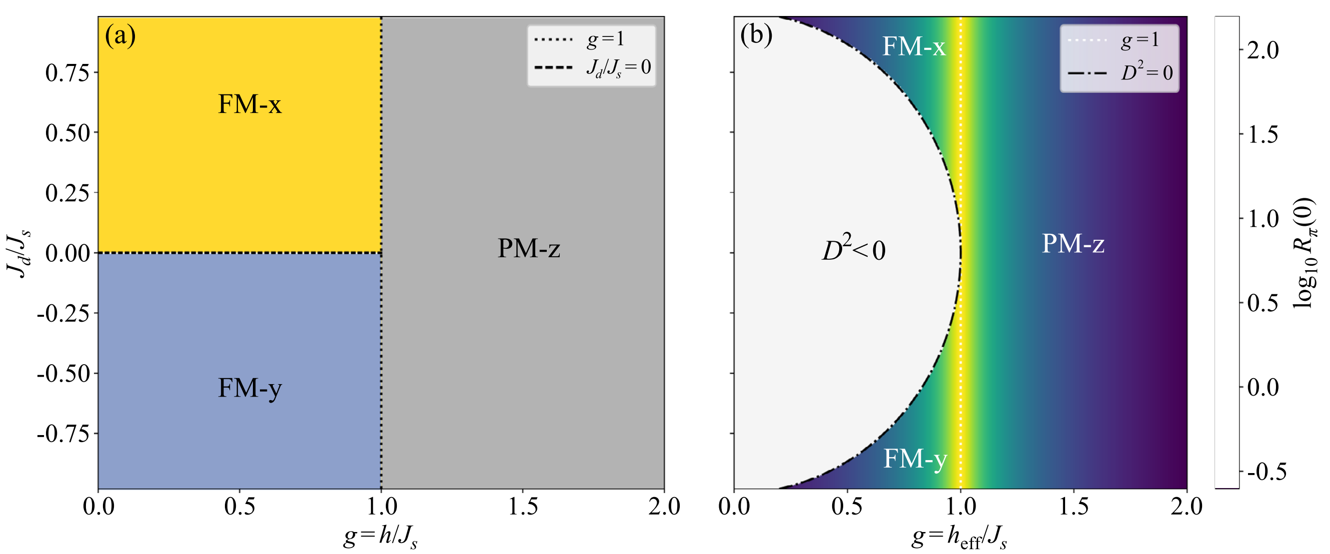

FIGURE 6 | Phase diagram of the XY model and its identification through a dissipative response of the DOPO network. (a) Phase diagram of the XY model in the parameter space $(g, J_d/J_s)$, where $g = h/J_s$. The regions $g < 1, J_d/J_s > 0$ and $g < 1, J_d/J_s < 0$ correspond to the FM-x and FM-y phases, respectively, while $g > 1$ corresponds to the PM-z phase. The dashed line denotes the critical line of the isotropic XY model, i.e., $J_d/J_s = 0$, and the dotted line marks the critical line, i.e., $g = 1$ or equivalently $h = h_c = J_s$. (b) Dissipative response map of the DOPO network, $\log_{10} R_\pi(0)$, expressed in the same normalized parameter space with $g = h_{\text{eff}}/J_s$. The bright vertical ridge centered at $g = 1$ represents the finite-linewidth enhancement of the $k = \pi$ mode and therefore locates the critical line of the mapped XY model. Combining the position relative to this ridge with the sign of J_d/J_s allows one to identify the corresponding phases of the XY model within the accessible region $D^2 \geq 0$. The black dash-dotted curve denotes the boundary with $D^2 = 0$, and the shaded region with $D^2 < 0$ is inaccessible to the present finite-parameter mapping of the DOPO network. Importantly, panel (b) is an optical response map rather than a thermodynamic phase diagram of the DOPO network itself.

25119044, 2026, 9, Downloaded from https://advanced.onlinelibrary.wiley.com/doi/10.1002/qute.70428 by Beijing Normal University, Wiley Online Library on [02/09/2026]. See the Terms and Conditions (https://onlinelibrary.wiley.com/terms-and-conditions) on Wiley Online Library for rules of use; OA articles are governed by the applicable Creative Commons License

x phase, while negative J_d/J_s leads to the FM-y phase. Once the normalized transverse field crosses the critical line $g = 1$, the system becomes z-polarized and enters the paramagnetic phase PM-z. The line $J_d/J_s = 0$ corresponds to the isotropic XY case. Figure 6b in contrast, is not a phase diagram of the optical system. It is a dissipative response map of the DOPO network, $\log_{10} R_\pi(0)$, in the same normalized parameter space, with the horizontal coordinate reconstructed from the detuning of the DOPO network as $g = h_{\text{eff}}/J_s$. The bright vertical ridge at $g = 1$ corresponds to the enhancement of the $k = \pi$ mode and therefore locates the critical line of the corresponding XY model. The black dash-dotted curve denotes the $D^2 = 0$ boundary, and the shaded region with $D^2 < 0$ is inaccessible to the present finite-parameter mapping of the DOPO network. Within the optically accessible region $D^2 \geq 0$, combining the position of the broadened soft-mode ridge with the sign of J_d/J_s allows one to infer the corresponding phase of the mapped XY model, i.e., the region $g < 1, J_d/J_s > 0$ corresponds to FM-x, the region $g < 1, J_d/J_s < 0$ corresponds to FM-y, and $g > 1$ corresponds to PM-z. Therefore, the dissipative DOPO network acts as a spectroscopic readout of the phase diagram of the XY. Figure 6b is not a thermodynamic phase diagram of the DOPO network itself, but rather an optical response map from which the phases of the corresponding XY model can be inferred.

4 | Conclusion

In this work, we established a spectral mapping between aone-dimensional XY spin chain and a network of coupled DOPOs. For finite $J_x > 0$ and $J_y > 0$, the mapping reproduces the spectrum of the XY model exactly and therefore encodes the gap closing at the quantum critical point in experimentally tunable optical parameters. We emphasize that the present construction has a well-defined domain of validity. For anisotropic couplings $J_x \neq J_y$, the mapped parametric drive is real only for $h \geq 2\sqrt{J_x J_y}$. Hence, the scheme directly accesses the critical point and a near-critical strong-field window, but does not generally reproduce the complete evolution from zero field through the entire ordered phase. The strict transverse-field Ising limit $J_y = 0$ is singular under the finite-parameter mapping. Nevertheless, a strongly anisotropic chain with $0 < J_y \ll J_x$ provides a quasi-TFI regime. When finite loss of the signal mode is included, the ideal gap-closing singularity is rounded into a finite-linewidth response peak. The peak becomes broader and lower as γ_s increases, while its center remains fixed by $\Omega_\pi = 0$, allowing the dissipative response of the DOPO to serve as a spectroscopic readout of the critical line of the mapped XY.

Accordingly, the principal result of this work is not a finite-parameter realization of the QPT of the XY model in the DOPO network itself, but a tunable photonic platform for spectrally emulating and detecting critical behavior of the corresponding XY family of the spin chains. The DOPO network remains in the same dynamically stable dissipative regime, while its spectrum and linear response encode the criticality of the mapped spin model. This approach may be extended to other spin models and higher-dimensional photonic networks, where optical nonlinearity and dissipation can provide additional routes for probing critical phenomena.

Acknowledgements

This work was supported by the National Natural Science Foundation of China under Grant No. 62461160263, Quantum Science and Technology-National Science and Technology Major Project (2023ZD0300200), and Guangdong Provincial Quantum Science Strategic Initiative under Grant No. GDZX2505004.

Conflicts of Interest

The authors declare no conflicts of interest.

Data Availability Statement

The data that support the findings of this study are available from the corresponding author upon reasonable request.

References

1. S. Sachdev, *Quantum Phase Transitions*, 2nd ed. (Cambridge: Cambridge University Press, 2011), https://doi.org/10.1017/CBO9780511973765.

2. M. J. Hwang, R. Puebla, and M. B. Plenio, "Quantum Phase Transition and Universal Dynamics in the Rabi Model," *Physical Review Letters* 115, no. 18 (2015): 180404, https://doi.org/10.1103/PhysRevLett.115.180404.

3. T. C. Hu, H. Q. Pi, S. X. Xu, et al., "Optical Spectroscopy and Band Structure Calculations of the Structural Phase Transition in the Vanadium-Based Kagome metal ScV_6Sn_6," *Physical Review B* 107, no. 16 (2023): 165119, https://doi.org/10.1103/PhysRevB.107.165119.

4. Z. Zhu, D. N. Sheng, and I. Sodemann, "Widely Tunable Quantum Phase Transition from Moore–Read to Composite Fermi Liquid in Bilayer Graphene," *Physical Review Letters* 124, no. 9 (2020): 097604, https://doi.org/10.1103/PhysRevLett.124.097604.

5. N. E. Myerson-Jain, S. Yan, D. Weld, and C.-K. Xu, "Construction of Fractal Order and Phase Transition with Rydberg Atoms," *Physical Review Letters* 128, no. 1 (2022): 017601, https://doi.org/10.1103/PhysRevLett.128.017601.

6. S. Arya, M. S. Laad, and S. R. Hassan, "Quantum Phase Transitions in Strained Graphene Due to the Interplay Between Spin Fluctuations and Anisotropic Band Structure," *Physical Review B* 96, no. 8 (2017): 085126, https://doi.org/10.1103/PhysRevB.96.085126.

7. Y. P. Zhang, G. Chen, and C. W. Zhang, "Tunable Spin–Orbit Coupling and Quantum Phase Transition in a Trapped Bose–Einstein Condensate," *Scientific Reports* 3, no. 1 (2013): 1937, https://doi.org/10.1038/srep01937.

8. J. Hertkorn, J.-N. Schmidt, F. Böttcher, et al., "Density Fluctuations across the Superfluid–Supersolid Phase Transition in a Dipolar Quantum Gas," *Physical Review X* 11, no. 1 (2021): 011037, https://doi.org/10.1103/PhysRevX.11.011037.

9. N. Maksimovic, D. H. Eilbott, T. Cookmeyer, et al., "Evidence For a Delocalization Quantum Phase Transition Without Symmetry Breaking in $CeCoIn_5$," *Science* 375, no. 6576 (2022): 76–81, https://doi.org/10.1126/science.aaz4566.

10. W. Wang and Z. S. Ma, "Real-Complex Quantum Phase Transition in Non-Hermitian Disorder-Free Systems," *Physical Review B* 106, no. 11 (2022): 115306, https://doi.org/10.1103/PhysRevB.106.115306.

11. S. Bhattacharyya, S. Dasgupta, and A. Das, "Signature of a Continuous Quantum Phase Transition in Non-Equilibrium Energy Absorption: Footprints of Criticality on Higher Excited States," *Scientific Reports* 5, no. 1 (2015): 16490, https://doi.org/10.1038/srep16490.

12. V. Vijayan, L. Chotorlishvili, A. Ernst, S. S. P. Parkin, M. I. Katsnelson, and S. K. Mishra, "Topological Dynamical Quantum Phase Transition in a Quantum Skyrmion Phase," *Physical Review B* 107, no. 10 (2023): L100419, https://doi.org/10.1103/PhysRevB.107.L100419.

13. A. Paviglianiti and A. Silva, "Multipartite Entanglement in the Measurement-Induced Phase Transition of the Quantum Ising Chain,"

25119044, 2026, 9, Downloaded from https://advanced.onlinelibrary.wiley.com/doi/10.1002/qute.70428 by Beijing Normal University, Wiley Online Library on [02/09/2026]. See the Terms and Conditions (https://onlinelibrary.wiley.com/terms-and-conditions) on Wiley Online Library for rules of use; OA articles are governed by the applicable Creative Commons License

Physical Review B 108, no. 18 (2023): 184302, https://doi.org/10.1103/PhysRevB.108.184302.

14. Y. C. Zhang, L. Vidmar, and M. Rigol, "Information Measures for a Local Quantum Phase Transition: Lattice Fermions in a One-Dimensional Harmonic Trap," *Physical Review A* 97, no. 2 (2018): 023605, https://doi.org/10.1103/PhysRevA.97.023605.

15. S. Sahu, S. L. Xu, and B. Swingle, "Scrambling Dynamics Across a Thermalization–Localization Quantum Phase Transition," *Physical Review Letters* 123, no. 16 (2019): 165902, https://doi.org/10.1103/PhysRevLett.123.165902.

16. M. Heyl, F. Pollmann, and B. Dóra, "Detecting Equilibrium and Dynamical Quantum Phase Transitions in Ising Chains via Out-of-Time-Ordered Correlators," *Physical Review Letters* 121, no. 1 (2018): 016801, https://doi.org/10.1103/PhysRevLett.121.016801.

17. Q. Ai, T. Shi, G. L. Long, and C. P. Sun, "Induced Entanglement Enhanced by Quantum Criticality," *Physical Review A* 78, no. 2 (2008): 022327, https://doi.org/10.1103/PhysRevA.78.022327.

18. E. Brillaux, A. A. Fedorenko, and I. A. Gruzberg, "Surface Quantum Critical Phenomena in Disordered Dirac Semimetals," *Physical Review B* 109, no. 17 (2024): 174204, https://doi.org/10.1103/PhysRevB.109.174204.

19. Z. Wu, T. I. Weinberger, A. J. Hickey, et al., "A Quantum Critical Line Bounds the High Field Metamagnetic Transition Surface in UTe_2," *Physical Review X* 15, no. 2 (2025): 021019, https://doi.org/10.1103/PhysRevX.15.021019.

20. H. J. Kim, F. Gay, A. Del Maestro, B. Sacépé, and A. Rogachev, "Pair-Breaking Quantum Phase Transition in Superconducting Nanowires," *Nature Physics* 14, no. 9 (2018): 912–917, https://doi.org/10.1038/s41567-018-0179-8.

21. W. T. He, C. W. Lu, Y. X. Yao, H. Y. Zhu, and Q. Ai, "Criticality-Based Quantum Metrology in the Presence of Decoherence," *Frontiers of Physics* 18, no. 3 (2023): 31304, https://doi.org/10.1007/s11467-023-1278-2.

22. S. B. Tang, H. Qin, B. B. Liu, et al., "Enhancement of Quantum Sensing in a Cavity-Optomechanical System Around the Quantum Critical Point," *Physical Review A* 108, no. 5 (2023): 053514, https://doi.org/10.1103/PhysRevA.108.053514.

23. J. H. Lü, W. Ning, X. Zhu, et al., "Critical Quantum Sensing Based on the Jaynes–Cummings Model With a Squeezing Drive," *Physical Review A* 106, no. 6 (2022): 062616, https://doi.org/10.1103/PhysRevA.106.062616.

24. L. Shao, R. Zhang, W. J. Lu, Z. C. Zhang, and X. G. Wang, "Quantum Phase Transition in the *XXZ* Central Spin Model," *Physical Review A* 107, no. 1 (2023): 013714, https://doi.org/10.1103/PhysRevA.107.013714.

25. T. L. Heugel, M. Biondi, O. Zilberberg, and R. Chitra, "Quantum Transducer Using a Parametric Driven-Dissipative Phase Transition," *Physical Review Letters* 123, no. 17 (2019): 173601, https://doi.org/10.1103/PhysRevLett.123.173601.

26. Q. Guan and R. J. Lewis-Swan, "Identifying and Harnessing Dynamical Phase Transitions for Quantum-Enhanced Sensing," *Physical Review Research* 3, no. 3 (2021): 033199, https://doi.org/10.1103/PhysRevResearch.3.033199.

27. M. Shafiei, F. Fazileh, F. M. Peeters, and M. V. Milošević, "Tuning the Quantum Phase Transition of an Ultrathin Magnetic Topological Insulator," *Physical Review Materials* 8, no. 7 (2024): 074201, https://doi.org/10.1103/PhysRevMaterials.8.074201.

28. H. Sun, S. S. Li, W. X. Ji, and C. W. Zhang, "Valley-Dependent Topological Phase Transition and Quantum Anomalous Valley Hall Effect in Single-Layer RuClBr," *Physical Review B* 105, no. 19 (2022): 195112, https://doi.org/10.1103/PhysRevB.105.195112.

29. M. Mogi, D. S. Choi, L. Primeau, et al., "Direct Observation of a Photoinduced Topological Phase Transition in Bi-Doped (Pb,Sn)Se," *Physical Review Letters* 133, no. 23 (2024): 236601, https://doi.org/10.1103/PhysRevLett.133.236601.

30. M. Kalinowski, R. Samajdar, R. G. Melko, M. D. Lukin, S. Sachdev, and S. W. Choi, "Bulk and Boundary Quantum Phase Transitions in a Square Rydberg Atom Array," *Physical Review B* 105, no. 17 (2022): 174417, https://doi.org/10.1103/PhysRevB.105.174417.

31. S. Yang and J. B. Xu, "Density-Wave-Ordered Phases of Rydberg Atoms on a Honeycomb Lattice," *Physical Review E* 106, no. 3 (2022): 034121, https://doi.org/10.1103/PhysRevE.106.034121.

32. T. Manovitz, S. H. Li, S. Ebadi, et al., "Quantum Coarsening and Collective Dynamics on a Programmable Simulator," *Nature* 638, no. 8049 (2025): 86–92, https://doi.org/10.1038/s41586-024-08353-5.

33. S. L. Zhu, "Scaling of Geometric Phases Close to the Quantum Phase Transition in the *XY* Spin Chain," *Physical Review Letters* 96, no. 7 (2006): 077206, https://doi.org/10.1103/PhysRevLett.96.077206.

34. S. S. Fu, X. H. Li, and S. L. Luo, "Detecting Quantum Phase Transition via Magic Resource in the *XY* Spin Model," *Physical Review A* 106, no. 6 (2022): 062405, https://doi.org/10.1103/PhysRevA.106.062405.

35. Z. Y. Sun, Y. Y. Wu, J. Xu, et al., "Characterization of Quantum Phase Transition in the *XY* Model With Multipartite Correlations and Bell-Type Inequalities," *Physical Review A* 89, no. 2 (2014): 022101, https://doi.org/10.1103/PhysRevA.89.022101.

36. F. W. Ma, S. X. Liu, and X. M. Kong, "Entanglement and Quantum Phase Transition in the One-Dimensional Anisotropic *XY* Model," *Physical Review A* 83, no. 6 (2011): 062309, https://doi.org/10.1103/PhysRevA.83.062309.

37. R. Grazi, D. Sacco Shaikh, M. Sassetti, N. Traverso Ziani, and D. Ferraro, "Controlling Energy Storage Crossing Quantum Phase Transitions in an Integrable Spin Quantum Battery," *Physical Review Letters* 133, no. 19 (2024): 197001, https://doi.org/10.1103/PhysRevLett.133.197001.

38. P. Nandi, S. Bhattacharyya, and S. Dasgupta, "Detection of Quantum Phase Boundary at Finite Temperatures in Integrable Spin Models," *Physical Review Letters* 128, no. 24 (2022): 247201, https://doi.org/10.1103/PhysRevLett.128.247201.

39. F. Pázmándi and Z. Domański, "Quantum Phase Transitions in *XY* Spin Models," *Physical Review Letters* 74, no. 12 (1995): 2363–2366, https://doi.org/10.1103/PhysRevLett.74.2363.

40. S. Zamani, R. Jafari, and A. Langari, "Floquet Dynamical Quantum Phase Transition in the Extended *XY* Model: Nonadiabatic to Adiabatic Topological Transition," *Physical Review B* 102, no. 14 (2020): 144306, https://doi.org/10.1103/PhysRevB.102.144306.

41. S. Ghosh and A. Sen(De)„ "Dimensional Enhancements in a Quantum Battery With Imperfections," *Physical Review A* 105, no. 2 (2022): 022628, https://doi.org/10.1103/PhysRevA.105.022628.

42. S. Ghosh, T. Chanda, S. Mal, and A. Sen(De), "Fast Charging of a Quantum Battery Assisted by Noise," *Physical Review A* 104, no. 3 (2021): 032207, https://doi.org/10.1103/PhysRevA.104.032207.

43. S. Satoori, S. Mahdavifar, and J. Vahedi, "Quantum Correlations in the Frustrated *XY* Model on the Honeycomb Lattice," *Scientific Reports* 13, no. 1 (2023): 16034, https://doi.org/10.1038/s41598-023-43080-3.

44. S. Y. Liu, Y. R. Zhang, W. L. Yang, and H. Fan, "Global Quantum Discord and Quantum Phase Transition in *XY* Model," *Annals of Physics* 362 (2015): 805–813, https://doi.org/10.1016/j.aop.2015.09.014.

45. G. A. P. Ribeiro and G. Rigolin, "Finite-Temperature Detection of Quantum Critical Points: A Comparative Study," *Physical Review B* 109, no. 24 (2024): 245122, https://doi.org/10.1103/PhysRevB.109.245122.

46. Z. Wang, A. Marandi, K. Wen, R. L. Byer, and Y. Yamamoto, "Coherent Ising Machine Based on Degenerate Optical Parametric Oscillators," *Physical Review A* 88, no. 6 (2013): 063853, https://doi.org/10.1103/PhysRevA.88.063853.

47. Y. Inui and Y. Yamamoto, "Entanglement and Quantum Discord in Optically Coupled Coherent Ising Machines," *Physical Review A* 102, no. 6 (2020): 062419, https://doi.org/10.1103/PhysRevA.102.062419.

48. K. Takata, A. Marandi, R. Hamerly, et al., "A 16-bit Coherent Ising Machine for One-Dimensional Ring and Cubic Graph Problems," *Scientific Reports* 6, no. 1 (2016): 34089, https://doi.org/10.1038/srep34089.

25119044, 2026, 9, Downloaded from https://advanced.onlinelibrary.wiley.com/doi/10.1002/qute.70428 by Beijing Normal University, Wiley Online Library on [02/09/2026]. See the Terms and Conditions (https://onlinelibrary.wiley.com/terms-and-conditions) on Wiley Online Library for rules of use; OA articles are governed by the applicable Creative Commons License

49. T. Inagaki, Y. Haribara, K. Igarashi, et al., "A Coherent Ising Machine for 2000-node Optimization Problems," *Science* 354, no. 6312 (2016): 603–606, https://doi.org/10.1126/science.aah4243.

50. P. L. McMahon, A. Marandi, Y. Haribara, et al., "A Fully Programmable 100-Spin Coherent Ising Machine With All-to-all Connections," *Science* 354, no. 6312 (2016): 614–617, https://doi.org/10.1126/science.aah5178.

51. N. Mwamsojo, F. Lehmann, K. Merghem, B.-E. Benkelfat, and Y. Frignac, "Optoelectronic Coherent Ising Machine for Combinatorial Optimization Problems," *Optics Letters* 48, no. 8 (2023): 2150–2153, https://doi.org/10.1364/OL.485215.

52. H. Takesue, K. Inaba, T. Honjo, et al., "Finding Independent Sets in Large-Scale Graphs With a Coherent Ising Machine," *Science Advances* 11, no. 7 (2025): eads7223, https://doi.org/10.1126/sciadv.ads7223.

53. K. Inaba, Y. Yamada, and H. Takesue, "Thermodynamic Quantities of Two-Dimensional Ising Models Obtained by Noisy Mean-Field Annealing and a Coherent Ising Machine," *Physical Review Applied* 20, no. 4 (2023): 044074, https://doi.org/10.1103/PhysRevApplied.20.044074.

54. T. Honjo, T. Sonobe, K. Inaba, et al., "100,000-Spin Coherent Ising Machine," *Science Advances* 7, no. 40 (2021): eabh0952, https://doi.org/10.1126/sciadv.abh0952.

55. H. Takesue, Y. Yamada, K. Inaba, et al., "Observing a Phase Transition in a Coherent Ising Machine," *Physical Review Applied* 19, no. 3 (2023): L031001, https://doi.org/10.1103/PhysRevApplied.19.L031001.

56. A. Yamamura, H. Mabuchi, and S. Ganguli, "Geometric Landscape Annealing as an Optimization Principle Underlying the Coherent Ising Machine," *Physical Review X* 14, no. 3 (2024): 031054, https://doi.org/10.1103/PhysRevX.14.031054.

57. Y. Mizuno and T. Komatsuzaki, "Finding Optimal Pathways in Chemical Reaction Networks Using Ising Machines," *Physical Review Research* 6, no. 1 (2024): 013115, https://doi.org/10.1103/PhysRevResearch.6.013115.

58. K. Terayama, M. Sumita, R. Tamura, and K. Tsuda, "Black-Box Optimization for Automated Discovery," *Accounts of Chemical Research* 54, no. 6 (2021): 1334–1346, https://doi.org/10.1021/acs.accounts.0c00713.

59. D. B. Kell, "Scientific Discovery as a Combinatorial Optimisation Problem: How Best to Navigate the Landscape of Possible Experiments?" *BioEssays* 34, no. 3 (2012): 236–244, https://doi.org/10.1002/bies.201100144.

60. H. Wei, C. J. Ai, P. T. Guo, et al., "A Versatile Coherent Ising Computing Platform," *Light: Science & Applications* 15, no. 1 (2026): 74, https://doi.org/10.1038/s41377-025-02178-1.

61. M. O. Scully and M. S. Zubairy, *Quantum Optics* (Cambridge: Cambridge University Press, 1997), https://doi.org/10.1017/CBO9780511813993.

62. A. Roy, S. Jahani, C. Langrock, M. Fejer, and A. Marandi, "Spectral Phase Transitions in Optical Parametric Oscillators," *Nature Communications* 12, no. 1 (2021): 835, https://doi.org/10.1038/s41467-021-21048-z.

63. A. Roy, R. Nehra, C. Langrock, M. Fejer, and A. Marandi, "Non-Equilibrium Spectral Phase Transitions in Coupled Nonlinear Optical Resonators," *Nature Physics* 19, no. 3 (2023): 427–434, https://doi.org/10.1038/s41567-022-01874-8.

64. A. A. Clerk, M. H. Devoret, S. M. Girvin, F. Marquardt, and R. J. Schoelkopf, "Introduction to Quantum Noise, Measurement, and Amplification," *Reviews of Modern Physics* 82, no. 2 (2010): 1155–1208, https://doi.org/10.1103/RevModPhys.82.1155.

25119044, 2026, 9, Downloaded from https://advanced.onlinelibrary.wiley.com/doi/10.1002/qute.70428 by Beijing Normal University, Wiley Online Library on [02/09/2026]. See the Terms and Conditions (https://onlinelibrary.wiley.com/terms-and-conditions) on Wiley Online Library for rules of use; OA articles are governed by the applicable Creative Commons License